Augmented Collisional Ionization in the VUV regime; a theoretical study

Nicolas Bigaouette* and Lora Ramunno†
Department of Physics, University of Ottawa, 150 Louis Pasteur, Ottawa ON, K1N 6N5, Canada

Edward Ackad‡
Department of Physics, Southern Illinois University Edwardsville, State Route 157 Edwardsville, IL 62026, United States

(Dated: February 7, 2013)

ABSTRACT

I. INTRODUCTION

The advance of Free Electrons Lasers (FEL) around the world gave access to unprecedented intensity at wide range of wavelengths, from infrared (IR) to X-ray. Recent experiments have studied the interaction of such laser pulses with clusters of atoms. These clusters are nanoscopic objects at solid density and as such, collective behaviour must not be ignored. Additionally, their finite size makes them easier to study, both theoretically and experimentally.

Many studies of the interaction of laser-matter have been done at wavelengths ranging from the IR to X-ray regimes. Experiments from Wabnitz *et al.*[1] with the FEL at DESY in 2002 on clusters of Xenon and VUV radiation saw anomalously high charge states (Xe^{8+}) using 98 nm (12.7 eV) pulses at an intensity of (what was though at the time) 7×10^{13} and 2×10^{13} W/cm^2.

These high charge states are due to the collective effects of ions and electrons at solid densities. Exactly which effects though is still debated. Four major models have emerged to explain the high ionization levels. First, the lowering of the potential barrier was suggested for photo-ionization [2–5]. Whereas, for example, two photons are normally necessary to ionize an ion, a neighboring ion lowers the barrier making the absorption of a single photon by the electron energetically possible.

Others have suggested using an "atomic potential" instead of the Coulomb potential. Santra and Green used a simple screening potential [6] and later a more realistic one [7] based on a Hartree-Fock-Slater code written by F. Herman and S. Skillman [8] and saw 30 times more VUV photons absorbed by a cluster environment compared with using a simple Coulomb potential and charge states up to Xe^{6+} for Xe_{1500} clusters.

The previous models describe single-[2, 5] and multi-[6, 7] photon ionization processes. Due to the high density of particles in a cluster environment, Jungreuthmayer *et al.*[9] identified an additional mechanism to inverse Bremsstrahlung heating (IBH) called "Multi-Body Recombination" (MBR) heating. Due to the high density and highly collisional nature of the plasma created in clusters by VUV laser pulses, electrons can cool down through collisions in the ion's potential well and recombine to a highly excited state. This newly recombined electron can then re-asbord a new photon from the laser, effectively increasing the system's total energy. Using a classical approach to the particles' dynamics, they observed high charge states up to 7+ for their highest intensity (7×10^{13} W/cm^2).

Lastly, our group suggested that atomic excited states might be extremely important for understanding the high charge states seen in cluster experiments [10, 11]. While our previous work was in the XUV regime (32.8 eV) and for Argon, the process of "Augmented Collisional Ionization" (ACI) is wavelength independent and can be applied to Xenon clusters as well.

In 2010, the intensity of the DESY-FEL pulses[1] was revised by Bostedt *et al.*[12] to a lower value of 8×10^{12} W/cm^2 instead of the previously though 2×10^{13} W/cm^2. In light of these new parameters, we propose revisiting this 2002 experiment using our ACI model.

In the first part of this paper, we will describe our classical approach to the clusters' dynamics followed by the different ionization processes which are treated quantum mechanically. The validation of our model is accomplished by comparing our results with [9]'s simulations results. We will then use our model to reproduce Wabnitz *et al.*'s and Bostedt *et al.*'s experimental results. Finally, we will look at the influence of the potential depth used throughout our simulations and its effect of the ionization spectrum.

II. MODEL

Clusters are nanoscopic systems and as such are hard to model using statistical approaches which often assume infinite systems. Our model thus tracks every particle present using a classical molecular dynamics (MD) code. Such MD codes are excellent tools for the simulation of a low number of particles since no approximation is used (apart from instantaneous electrostatic interactions). Unfortunately, the N-body interaction has an $O(N^2)$ scaling which renders simulations of more than

* nbigaouette@gmail.com
† lramunno@uottawa.ca
‡ eackad@uottawa.ca

tens of thousands of particles using long range interactions virtually impossible. Approximation to the N-body problem are possible; hierarchical tree code [13] and fast-multipole methods [14] can reduce the burden to an $O(N \log(N))$ problem.

These algorithms have overheads which makes them slower for a low number of particles. They can also introduce some errors in the force and potential calculations. While these errors are not significant for the dynamics aspect of the simulation, they can influence the calculated rates of quantum transitions used throughout the code.

Instead of using tree-based algorithms, we decided to port the classical dynamics aspect of the simulation to the OpenCL framework. This allows us to accelerate calculation on general-purpose graphical processing units (GP-GPU) similarly to Nvidia's CUDA. Contrary to the later, OpenCL is not bound to specific hardware vendor or even accelerator devices. For example, multi-core CPUs can also be used to accelerate calculation, making the code portable to many different architectures. It is not uncommon to see speedups of the order of 100 using GPGPUs. In our case, a speedup between 40 and 80 was seen when using an Nvidia GTX 580 GPU and our group's computer cluster with 20 Nvidia Tesla C2075 was used for the present work.

The Coulomb interaction between particles is cut at small distances to mitigate numerical heating. Particles are treated as gaussian charge densities where the potential is given by:

$$\phi(r) = \frac{Z}{r}\mathrm{erf}\left\{\frac{r}{\sigma\sqrt{2}}\right\} \tag{1}$$

with erf{} the error function, Z the charge state of the particle and σ the width of the charge density given by:

$$\sigma = \frac{Z}{D}\sqrt{\frac{2}{\pi}} \tag{2}$$

The maximum depth of the potential of a $Z = 1$ ion is given by D. Note that at large distances r, this smoothed potential converge to the Coulomb potential:

$$\phi(r >> \sigma) = \frac{Z}{r} \tag{3}$$

A. Heating Mechanisms

Initially, the simulated cluster is neutral. As time passes, the laser's energy, modeled as both an oscillating electric field with a carrier envelope and a flux of photons, is absorbed. Electrons are created in the code and their movement, as the new ions', is calculated classically. Many mechanisms, described next, play an important role in the energy absorption and diffusion throughout the cluster.

1. Single photon ionization

Since initially the cluster is neutral, the first step to ionization is the absorption of photons. At the studied intensities (10^{12} to 10^{13} W/cm^2) and wavelengths (98 nm), field ionization (tunnelling) is negligible, as is multi-photon ionization.

The laser is treated as a photon probability distribution following the intensity profile which is depleted as photons are absorbed. Experimental cross sections for Xenon in the VUV regime were taken from experimental data [15]. These cross-sections are converted to rates and a Monte-Carlo test evaluates the ionization probability.

New electrons then move freely in the cluster environment with an initial energy being the photon's minus the ionization potential (Ip).

Note that a 98 nm (12.7 eV) photon can directly ionize a neutral Xenon (with an Ip of 12.27 eV) but not a Xe^{1+} (with an Ip of 21.4 eV). Single photon ionization can thus not explain the high charge states seen in experiments by itself.

2. Impact ionization

Once electrons are created in the simulations they will impact atoms, ions and other electrons. While the later is treated as a classical collision, the former can result in the creation of extra electrons through impact ionization.

Impact ionization is implemented using the semi-empirical Lotz cross-sections [16] with parameters taken from [17] for the neutral and [18] for ionized Xenon. As for single photon ionization, the cross-sections are converted to rates which is used in a Monte-Carlo test for ionization probability.

The impacting electron must have enough kinetic energy to overcome the ionization barrier, which is taken care by having a null cross-section for lower energy impact. Additionally, the Lotz cross-section definition uses electron kinetic energy at infinity. Since the impacting electron is close to the atom (or ion), its potential energy with respect to that said ion is added to its kinetic energy to approximate its value at infinity. Furthermore, the cluster environment will influence the ionization threshold; this is approximated by the potential value at the ion's location (V_p, see figure 1). If the resulting effective kinetic energy is greater then the Ip, the ionization probability is calculated. In instances when the Monte-Carlo test succeeds, a new electron is created in the simulation and energy is removed from the impacting electron. Figure 1 shows the potential of two ions in blue (left) and red (right) dashed curves and the total potential in straight black line. For the ion on the left, the "cluster environment" V_p is approximated as the potential at the ion's location due to all other particles, excluding nearby electrons. The impacting electron is shown as the blue dot with a kinetic, potential and total energy in green. The electron's total energy with respect to the threshold

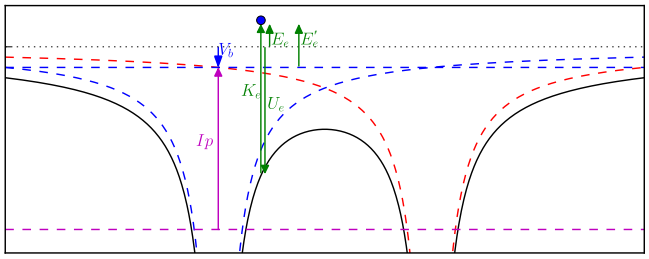

FIG. 1: Impact ionization schematic: an electron (blue dot, colours online) impact the ion on the left. It's total energy with respect to the cluster threshold V_p is compared against the ion's Ip (magenta).

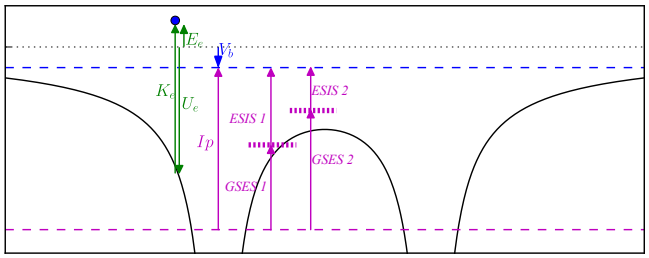

FIG. 2: Excited states in magenta (colours online) allows reaching the continuum through intermediate steps in the ACI model. GSES: Ground State to Excited State energy. ESIS: Excited State to Ionised State (continuum) energy.

V_p is shown as E'_e. It is this value E'_e which is compared to the Ip (in magenta) for impact ionization calculation.

3. Excited States (ACI)

We introduced a novel model [11] which we dubbed "Augmented Collisional Ionization" (ACI) that successfully described the high charge states seen in previous Argon experiments at 32 nm [19]. We believe ACI plays a critical role in the clusters ionization and the subsequent dynamics.

In the ACI model, electrons are created in a two step process. Similarly to impact ionization described above, an electron collides with the atom or ion. In contrast with impact ionization, the final state is not an ion plus two electrons but a single electron and an excited atom or ion. Once excited, an atom or ion can be impact-ionized more easily by a second, lower energy, electron. Figure 2 shows two intermediate accessible excited states for an ion. On average, the electron kinetic energy distribution in a cluster is approximately Maxwell-Boltzmann. By using this two steps process, electrons in the lower energy spectrum of the Maxwell-Boltzmann distribution can also contribute to the cluster ionization. Additionally, more ionization paths are present in the model.

ACI is modeled similarly to impact ionization. Cross sections for the different transitions are taken from a Hartree-Fock implementation of the Cowan code[20]. Due to the finite nature of computers, only the transitions cross-sections of a subset of all infinite number of excited states are calculated. For this work on Xenon clusters, eight excited states ($l < 4$) per charge state are used, for ionization levels up to Xe^{17+}. We emphasize that this a lower bound on the effect of ACI; the inclusion of more excited states would increase the effect.

B. Recombination

During the laser pulse, ACI has a strong effect on the maximum charge state. However, ionization is balanced by the recombination of electrons during the expansion and cooling of the created plasma. When an electron's total energy with respect to the V_p threshold becomes lower than the (recombination) Ip due to collisions, this electron is recombined with the parent ion and disappear from the simulation. The ion's charge state is updated to reflect the process.

This allows having a potential that is as close as Coulombic as possible (except at really close range where the potential converges to $\phi = ZD$) without having electrons with classical energy below the recombination Ip. Interestingly, it also accelerate the $O(N^2)$ force calculation by reducing the number of particles in the system.

C. Many Body Recombination

Our group proposed [9] another interesting heating process called "Many Body Recombination" (MBR). Through collisions, some free electrons will cool by transferring their energy to other electrons (the ions are considered fixed on the time scale of the electron dynamics). By falling into the ions potential these cooled electrons are said to recombine into a highly excited state where they can absorb more photons and thus more energy from the laser.

It was shown in [9] that MBR is a dominant energy absorption mechanisms in the VUV and cannot be ignored. MBR is automatically included in a classical MD simulation and is thus included in our results.

An important distinction between MBR and ACI is the direction in which the electronic transition takes place. In the case of ACI, the transition is going "up the energy ladder": a bound electron first in the ground state will receive energy from an impacting electron. Afterwards, the excited atom is ionized more easily by other impacting electrons due to, firstly, the cross-section of the excited state to continuum state being larger than the cross-section from the ground state to continuum. Secondly, the energy required for the excited state to continuum transition is less than that of the ground state to continuum transition and as such more free electrons have a chance to ionize the excited atom. On the other hand, MBR is a transition from the continuum to a highly

excited state. While the later is treated purely classically, the former is implemented using cross-sections taken from a Hartree-Fock calculation. The lower excited states used in ACI are distant from each other and must be treated discretely while the higher states in MBR are so dense that their classical treatment does not result in much error. Additionally, while ACI is independent of the laser field and only describes electron-ion collisions, the laser plays an active role in MBR.

III. RESULTS

A. Model validation

We first compare with data from Jungreuthmayer *et al.*[9]. Simulations were run at 1.5×10^{12} W/cm^2 and 1.5×10^{13} W/cm^2 for a cluster size of Xe_{1000} and 2×10^{13} W/cm^2 for Xe_{80}. Similarly to reference [9], the Coulomb potential is cut-off at close range to prevent the large field close to the discontinuity to cause numerical heating. Equation (1) is used for the cut-off with $D = 12$ eV. Such a shallow value is used to compare with previous publications where recombination is not present. Even though an electron orbiting in a Coulomb potential can have a range of energy from zero to minus infinity in a classical simulation, fixing the maximum depth of the potential to 12 eV prevents the orbiting electron from having a classical energy less than the recombination energy. Allowing an electron to have an energy below this recombination threshold value would also allow the electron to transfer its energy to other particles, artificially heating the system. This problem is prevented by simply choosing a potential depth D close to the ionization potential of the neutral Xenon.

When irradiated with a 98 nm (12.7 eV) laser pulse, the cluster becomes fully ionized rapidly. This is due to the fact that single photon ionization cross-section is largest (68 Mb) at longer wavelength for neutral Xenon. Since the photon energy is not sufficient to ionize a Xe^{1+} to a Xe^{2+}, only the first charge state is accessible through single photon ionization. Larger charge states are caused by other mechanisms as is evidenced by experiments with gas targets.

The small nature of these clusters, the random process of the Monte-Carlo ionization procedures and the chaotic nature of the many-body problem requires acquiring a large sample for valid statistics; for the Xe_{80}, 5,000 simulations were run for both ACI disabled and enabled. The simulation duration is 300 fs, after which the clusters continue their expansion without changing the charge states distribution. The laser pulse, with a full-width at half-max duration of 100 fs, has left the cluster after approximately 250 fs.

The highest charge state observed with ACI disabled is Xe^{4+} similar to the results of [9]. While the charge state spectrum shape is different than the data shown by Jungreuthmayer *et al.*, we note that the simulated parameters are not exactly the same and explain the small differences. For example, the smoothed Coulomb potential used in reference [9] is different than the one used here; see equation (1). Additionally, ionization cross-sections used in both works differs: for single photon ionization, photoabsorption cross-sections in the one electron approximation [21] was used by Jungreuthmayer *et al.*while experimental cross-sections from reference [15] were used here. For impact ionization, we refined the cross-sections by using the experimental data from references [17] and [18] rather than Lotz values [16]. We also note that 10,000 simulations were run for this parameter set (5,000 with ACI, 5,000 without). Finally, the many-body problem being a chaotic system, statistical deviations are to be expected.

When ACI is enabled, the highest charge state jumps to Xe^{6+}, two more than without ACI.

We also measured the number of electrons which are in a Many-Body Recombination (MBR) state. We found that around 18 % of the total number of electrons are in an MBR state, close to the value from reference [9] (around 25 %).

Furthermore, different intensities were simulated for Xe_{80} clusters. We found a highest charge state of Xe^{3+} (without ACI) and Xe^{5+} (with ACI) at 1.5×10^{12} W/cm^2 and Xe^{4+} (without ACI) and Xe^{6+} (with ACI) at 1.5×10^{13} W/cm^2. At both intensities, the most abundant charge state is the Xe^{1+} (without ACI) and Xe^{2+} (with ACI). Note that Jungreuthmayer *et al.* did not report these intensities for Xe_{80} clusters and so figures are not shown.

We also looked at Xe_{1000} clusters irradiated with a 1.5×10^{13} W/cm^2 laser pulse. The charge state distribution profile shows similarities as reference [9]; the largest charge state is Xe^{5+} and the most abundant is the Xe^{2+} (as opposed to Xe^{3+}) when ACI is disabled. The larger systems are computationally more intensive so only 100 runs of both ACI enable and disable were performed, still a larger sampling than the few runs by Jungreuthmayer *et al.*due to the limited computational infrastructure available at the time. The effect of ACI is to increase, by two, both the highest charge state obtained and the most abundant one, a clear indication that ACI has a central role amongst the ionization channels.

At 1.5×10^{12} W/cm^2, the spectrum distribution is similar to the one at 1.5×10^{13} W/cm^2. The largest charge state seen is Xe^{5+} (without ACI) and Xe^{6+} (with ACI). Note that for both with and without ACI, the largest charge state population seen at 1.5×10^{12} W/cm^2 is two orders of magnitude less than the previous state.

B. Revisiting the 100nm experiment

We will now compare our model with the VUV experiment [1, 12] at DESY with the revised intensity of 8×10^{12} W/cm^2. We will use the same potential depth of 12 eV as before to extract the influence of ACI on the

Distance to focus	Normalized height	Intensity ($\times 10^{12}$ W/cm^2)
0	1	8.000
$\sqrt{-2\sigma^2 \ln\left(\frac{1+e^{-1/2}}{2}\right)}$	$\frac{1+e^{-1/2}}{2}$	6.424
σ	$e^{-1/2}$	4.852
$\sigma\sqrt{2\ln(2)}$	1/2	4.000
$\sqrt{2}\sigma$	e^{-1}	2.943
2σ	e^{-2}	1.083

TABLE I: Intensity of pulse at different distances of the focus assuming a gaussian spatial profile with a standard deviation σ.

laser-cluster interaction. Similarly to the previous section, recombination is disabled and successive runs with ACI disabled and enabled are compared.

We assume here that the density of clusters coming out of the nozzle is constant in space over the whole laser focus. As such, the clusters distributed across the focus' spatial profile will sample a different laser intensity depending on their distance from the focus' centre. This is taken into account by running many different simulations at different intensities. Each intensity is then weighted accordingly to represent the different location in the laser's focus two dimensional cross section profile.

The peak intensity of the experiment being 8×10^{12} W/cm^2, we chose the values for the simulations shown on table I. Considering a focus diameter (FWHM) of $\tau = 20\mu$m we have $\sigma = \tau\left(2\sqrt{2\ln(2)}\right)^{-1} = 11.77\mu$m.

Figure 3 shows the charge state distribution for Xe_{90} clusters and figures 4, 5 and 6 show the distribution of icosahedral clusters with their 7$^{\text{th}}$, 8$^{\text{th}}$ and 11$^{\text{th}}$ closed shells (Xe_{1415}, Xe_{2057} and Xe_{5083}, respectively). All icosahedral configurations were relaxed using a Lennard-Jones potential for neutral xenon. On each figure, the left histogram is with ACI disabled and the right histogram is with ACI enabled. Since recombination is turned off, the dynamics of the cluster after the laser pulse is mainly expansion of the cluster; there is no significant ionization taking place in that regime. As such, simulations were run up to 400 fs which is approximately 150 fs after the end of the laser pulse. We have not seen any major changes when continuing the simulations to longer times.

It is important to remember here that there is no recombination during the simulation. As such, the number of electrons can only increase. While interesting to study the dynamics during the laser pulse, special care needs to be taken when comparing with experiments. Indeed, during the expansion of the cluster (between the end of the laser pulse and the detection on the time-of-flight (TOF) spectrometer) the created plasma will cool down and many electrons will recombine. One cannot thus simply compare the charge state spectrum generated by

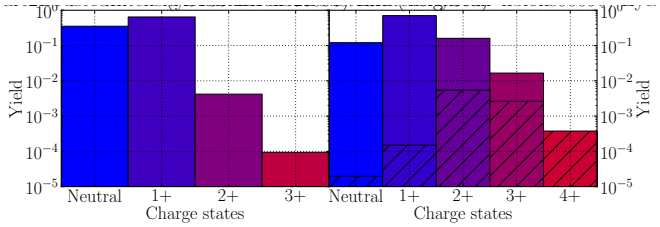

(a) Part 2: Xe_{90} (log scale)

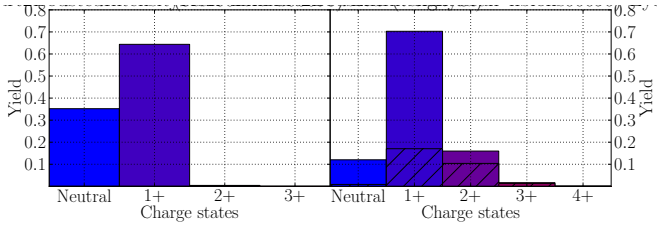

(b) Part 2: Xe_{90} (linear scale)

FIG. 3: Part 2: Xe_{90}

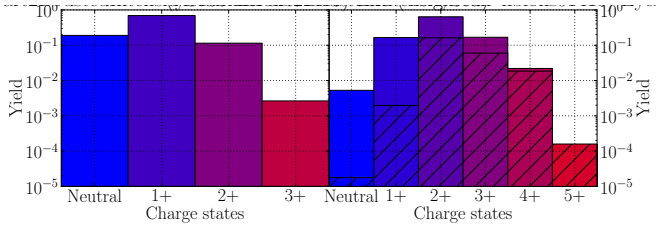

(a) Part 2: Xe_{1415} (log scale)

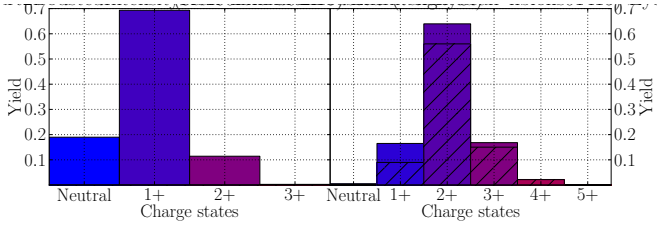

(b) Part 2: Xe_{1415} (linear scale)

FIG. 4: Part 2: Xe_{1415}

a simulation and one measured in a TOF. To reduce this difference between the two spectrums, we recombine, at the end of every simulations, electrons that are close to an ion and have a negative energy. This energy is calculated as the electron's kinetic energy plus the potential energy between this electron and the nearby ion. Once this recombination is done, the spectrum is calculated and plotted on figures 3, 4, 5 and 6.

We also note that neutral atoms are not detected by the TOF apparatus as the ions are accelerated toward the detector by an electric field which has no effect on neutrals; a direct comparison of the neutral population is thus not possible here.

Each figure show the results of our simulations using the same parameters as the DESY-FEL experiment [1, 12] and all intensities shown on table I. For the smallest

Size	Charge states yield (%)				
	Xe	Xe^{1+}	Xe^{2+}	Xe^{3+}	Xe^{4+}
1415	20.0	73.1	12.1	0.278	-
2057	17.4	73.1	14.5	0.350	0.00776
5083	11.8	69.4	18.1	0.587	0.0129

TABLE II: Charge states yield (%) with ACI disabled

Size	Charge states yield (%)					
	Xe	Xe^{1+}	Xe^{2+}	Xe^{3+}	Xe^{4+}	Xe^{5+}
1415	0.556	17.4	67.4	17.7	2.32	0.0162
2057	0.387	13.1	64.5	21.4	2.94	0.0336
5083	0.161	6.72	59.9	28.8	4.43	0.0392

TABLE III: Charge states yield (%) with ACI enabled

cluster size (Xe_{90} on figure 3), ACI increases the highest charge states by one, from Xe^{3+} to Xe^{4+}. For the next larger clusters (Xe_{1415}), ACI increases the highest charge state observed by two, from Xe^{3+} to Xe^{5+}. Finally, the two largest cluster sizes (Xe_{2057} and Xe_{5083}) see their largest charge state increase from Xe^{4+} to Xe^{5+} when ACI is enabled.

Additionally, the most abundant charge state is shifted from Xe^{1+} to Xe^{2+} when ACI is enabled for large clusters, while staying at Xe^{1+} for the smallest (Xe_{90}) clusters.

Figures 3, 4, 5 and 6 are in good agreement with the experiments [1, 12]: the dominant charge states seen was Xe^{2+} for the largest clusters ($Xe_{90,000}$) while for the smallest (Xe_{70}) the Xe^{1+} ion was dominant.

We can see that figures 4, 5 and 6 are quite similar except from the fact that the distribution is shifting to larger values as the cluster size increases. Without ACI, the populations of Xe^{3+} goes from 0.28 to 0.35 to 0.59 percent as the cluster size increase from Xe_{1415} to Xe_{2057} to Xe_{5083}. The Xe^{3+} population doubles between the Xe_{1415} and Xe_{5083} clusters. This is summed up on table II, while the same data with ACI enabled is shown on table III.

Even though Xe_{5083} clusters are less than four times larger than Xe_{1415}, they have 4 more closed shells. The doubling of the Xe^{3+} is likely caused by the number of ions on the cluster surface increasing more slowly than the number of ions in the cluster volume. For example, the Xe_{1415} clusters have 35 % of atoms inside their volume, while this proportion drops to 24 % for Xe_{5083}. Since we have seen that the higher charge states reside on the cluster boundaries, as reported in [10], we expect to see a slower increase of the yield of the highest charge states compared to the cluster size increase.

The extra charge states seen in these figures when ACI is enabled indicates that it plays a central role but, as we'll see in the next section, another aspect of the model must be explored to explain the high charge states seen in reference [12].

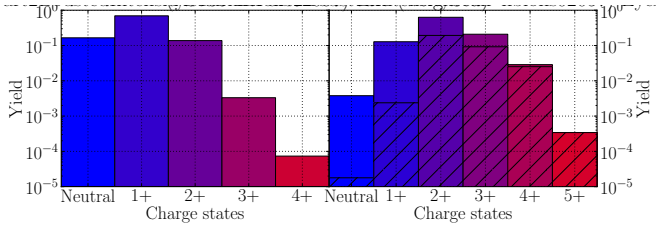

(a) Part 2: Xe_{2057} (log scale)

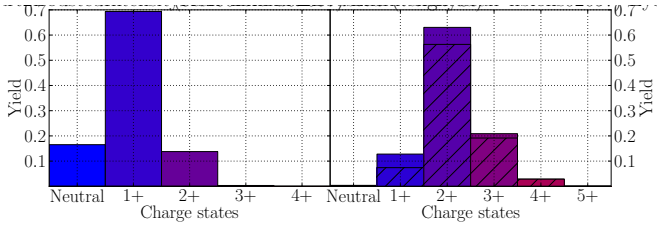

(b) Part 2: Xe_{2057} (linear scale)

FIG. 5: Part 2: Xe_{2057}

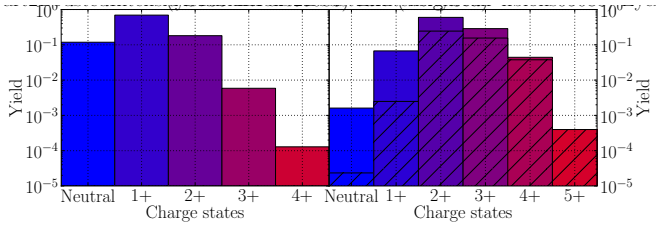

(a) Part 2: Xe_{5083} (log scale)

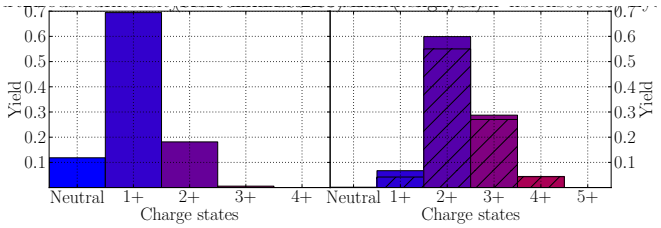

(b) Part 2: Xe_{5083} (linear scale)

FIG. 6: Part 2: Xe_{5083} (13 runs per figure)

C. Deeper potential

In the previous sections, data was collected for relatively shallow Coulomb-screening potential depth. This allowed keeping a reasonably large time step. However, we saw an interesting trend in the data; the potential depth used in the simulations would influence greatly the resulting charge states distribution.

Since the choice of potential depth is arbitrary (when recombination is used), we measured the Inverse Bremsstrahlung Heating (IBH) of a pre-ionized Xe_{147} cluster for different potential depth. Figure 7 shows the resulting energy absorption. As can be seen, the potential depth of less than 3 Hartree underestimate the amount of energy absorbed by the cluster. The energy absorption increases a lot after 3 Hartree but we suspect this

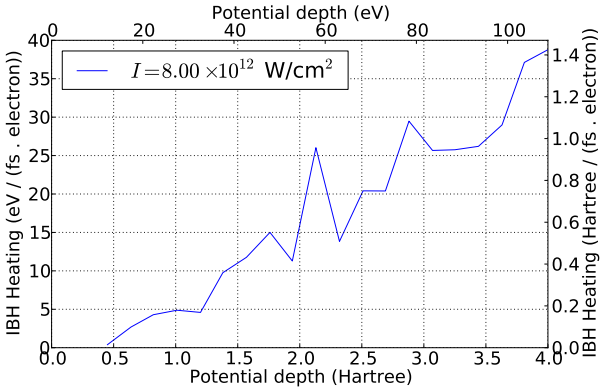

FIG. 7: Part 3: IBH, Xe_{147}

is due to numerical heating. Note that as the potential gets deeper, the field close to the ion increases and a smaller time step must be used. For such deep potential (3 Hartree ≈ 82 eV), the limit on the floating point precision of the computer becomes apparent and decreasing the time step used does not decrease the error anymore. Additionally, simulations using a time step smaller than 0.05 attosecond becomes intractable as the simulation time increases to many months. We have thus settled on a potential depth of 3 Hartree with a time step of 0.15 as which minimizes the calculation error while still providing reasonable simulation duration. We compared the following results with a time step of 0.1 as and found only negligible differences in the charge states distribution. Additionally, since electrons can now go bellow the ionization potential, recombination must to be enabled.

Figures 8 and 9 show the charge states distribution of Xe_{80} and Xe_{1415} clusters using the potential depth of 3 Hartree illuminated with a laser pulse of intensity 8×10^{12} W/cm^2. Note that due to the smaller time step used in this section not as many runs could be performed as was done in the previous section; 60 runs with ACI disabled and 60 others for ACI enabled were used to generate figure 8 while just one is shown on figure 9 as each run took a month. Additionally, both figures 8 and 9 are run up to 1 picosecond since the cluster continues to evolve even after the laser pulse is passed. This is mainly due to recombination.

As seen on figures 8 and 9, enabling ACI shifts the spectrum; more ions at high ionization state are present with ACI. Nevertheless, we see that the potential depth had an important influence on the results. While using a shallow potential shape like in the previous section gives a maximum charge states seen of Xe^{6+} for the largest cluster (Xe_{5083}) and ACI enabled, a potential almost seven times deeper (3 Hartree = 81.2 eV compared to 12 eV) gives similar results even for small clusters (Xe_{5083}) and with ACI disabled; enabling it still increases the ionization and shifts the distributions to higher charge states.

Additionally, we do see on figure 9 a drop in yield from Xe^{8+} to Xe^{9+}, similarly to reference [12], even though the experimental data is for much larger clusters ($Xe_{90,000}$).

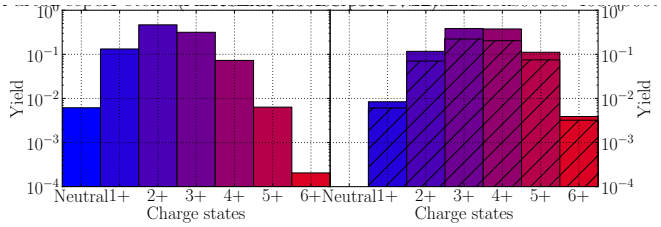

(a) Part 3: Xe_{80}, 8×10^{12}W/cm^2 (log scale)

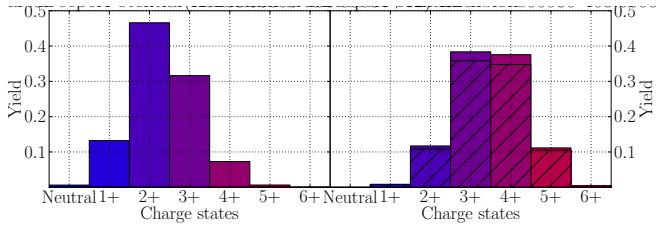

(b) Part 3: Xe_{80}, 8×10^{12}W/cm^2 (linear scale)

FIG. 8: Part 3: Xe_{80}, 8×10^{12}W/cm^2 (61 runs per figure)

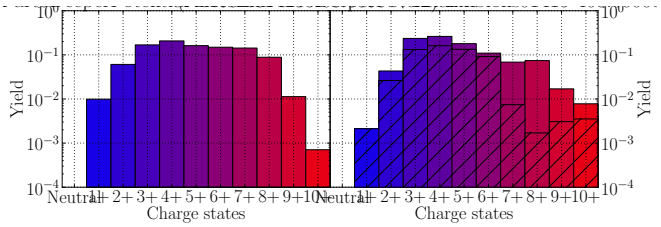

(a) Part 3: Xe_{1415}, 8×10^{12}W/cm^2 (log scale)

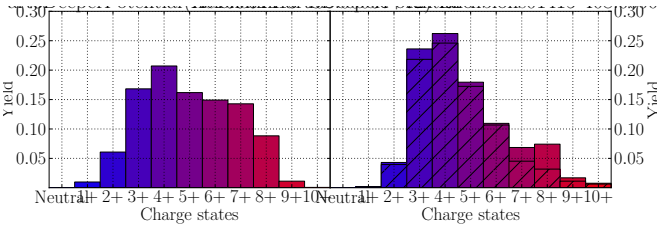

(b) Part 3: Xe_{1415}, 8×10^{12}W/cm^2 (linear scale)

FIG. 9: Part 3: Xe_{1415}, 8×10^{12}W/cm^2 (∼1ps)

IV. CONCLUSION

In summary, many refinements were made on previous models. For example, a smoother shape of the close range potential was used, removing the need for extremely small time steps to keep numerical heating under control. Additionally, the classical dynamics part of the code was re-written to run on GP-GPU for a 40 to 80 times speed increase. This allowed us to increase the number of simulations we ran and thus their statistical significance. We could also explore the laser intensity profile by running different simulations at different intensities, proportional to the focal cross section area.

Furthermore, better approximations were made for both single photon and collisional ionization by directly

using experimental cross-sections. More importantly, we applied our ACI model that was developed at a different wavelength regime but could still be used in the VUV.

We first compared the effect of ACI against previous simulations of Xe_{80} at 98 nm and 2×10^{13} W/cm^2. We have shown that using ACI resulted in two more charge states seen. Different intensities (1.5×10^{12} W/cm^2, 1.5×10^{13} W/cm^2) and a different cluster size (Xe_{1000}) were also used and gave similar results; two more charge states are obtainable with ACI.

Afterwards, we revisited an important experiment that took place in 2002 at the DESY-FEL installations in Hambourg, Germany, where xenon clusters of different sizes were illuminated by a 98 nm laser pulse. Initially, the laser intensity was though to be 2×10^{13} W/cm^2 but has been subsequently reduced to 8×10^{12} W/cm^2 after re-calibration.

ACI did increases the highest charge state seen by either one or two values and the most abundant ionization state by just one state (depending on the cluster sizes). In the small clusters (Xe_{90}), only when ACI was enabled that the same charge state spectrum as the DESY experiment could be obtained; both largest state seen and most abundant one (Xe^{4+} and Xe^{1+}, respectively) match the experimental data.

For computational reasons, the largest clusters that could be simulated were Xe_{5083}. While tricky to compare with the $Xe_{90,000}$ of the experiment, we did saw a slow increase in the population of high charge state as the cluster size increased. The experimental data does not show at which cluster size the transition between a most abundant charge state of Xe^{1+} to Xe^{2+} takes place, but we do see this at Xe_{1415} in our simulations (with ACI enabled). Without ACI, we did not see that transition at all, a strong indication that ACI is an important effect that cannot be neglected.

The DESY experiment saw up to Xe^{8+} for the largest cluster size ($Xe_{90,000}$) which we could not simulate. It is not clear to us if the cluster size increase would show the increased charge states up to Xe^{8+}; four times the cluster size (from Xe_{1415} to Xe_{5083}) just doubled the yield of Xe^{5+}. Does increasing by sixty times the cluster size able to increase not only the yield of Xe^{5+} but most importantly attain the Xe^{8+}? This is still an open question.

We also explored the potential depth used during the simulation and have found that at seven times deeper, Xe_{1415} clusters can show interestingly high charge states. These results open the door the further studies of the effect of potential depth used in MD calculations. Other groups studied the effect of an atomic potential instead of a pure Coulombic one and found interesting results. This atomic potential could be implemented later on in future works.

[1] H. Wabnitz, L. Bittner, A. R. B. de Castro, R. Dhrmann, P. Grtler, T. Laarmann, W. Laasch, J. Schulz, A. Swiderski, K. von Haeften, T. Mller, B. Faatz, A. Fateev, J. Feldhaus, C. Gerth, U. Hahn, E. Saldin, E. Schneidmiller, K. Sytchev, K. Tiedtke, R. Treusch, and M. Yurkov, Nature **420**, 4825 (2002).

[2] C. Siedschlag and J.-M. Rost, Physical Review Letters **93**, 43402 (2004).

[3] U. Saalmann and J.-M. Rost, Physical Review Letters **91** (2003), 10.1103/PhysRevLett.91.223401.

[4] U. Saalmann, C. Siedschlag, and J.-M. Rost, Journal of Physics B: Atomic, Molecular and Optical Physics **39**, R39R77 (2006).

[5] I. Georgescu, U. Saalmann, and J.-M. Rost, Physical Review A **76**, 18 (2007).

[6] C. Greene and R. Santra, Physical Review Letters **91**, 14 (2003).

[7] R. Santra and C. Greene, Physical Review A **70** (2004), 10.1103/PhysRevA.70.053401.

[8] F. Herman and S. Skillman, *LANL* (Prentice-Hall, 1963).

[9] C. Jungreuthmayer, L. Ramunno, J. Zanghellini, and T. Brabec, Journal of Physics B: Atomic, Molecular and Optical Physics **38**, 30293036 (2005).

[10] E. Ackad, N. Bigaouette, K. Briggs, and L. Ramunno, Physical Review A **83**, 063201 (2011).

[11] E. Ackad, N. Bigaouette, and L. Ramunno, Journal of Physics B: Atomic, Molecular and Optical Physics **44**, 165102 (2011), arXiv:1011.5216.

[12] C. Bostedt, M. Adolph, E. Eremina, M. Hoener, D. Rupp, S. Schorb, H. Thomas, A. R. B. de Castro, and T. Mller, Journal of Physics B: Atomic, Molecular and Optical Physics **43**, 194011 (2010).

[13] J. E. Barnes and P. Hut, Nature **324**, 446449 (1986).

[14] P. Gibbon and G. Sutmann, in *Quantum Simulations of Complex Many-Body Systems: From Theory to Algorithms*, NIC Series, Vol. 10 (2002) p. 467506.

[15] J. B. West and J. Morton, Atomic Data and Nuclear Data Tables **22**, 103107 (1978).

[16] W. Lotz, Zeitschrift fur Physik **206**, 205211 (1967).

[17] H. Tawara and T. Kato, Atomic Data and Nuclear Data Tables **36**, 167353 (1987).

[18] A. Heidenreich, I. Last, and J. Jortner, The European Physical Journal D **35**, 567577 (2005).

[19] C. Bostedt, H. Thomas, M. Hoener, E. Eremina, T. Fennel, K.-H. Meiwes-Broer, H. Wabnitz, M. Kuhlmann, E. Plonjes, K. Tiedtke, R. Treusch, J. Feldhaus, A. R. B. de Castro, and T. Moller, Physical Review Letters **100**, 133401 (2008).

[20] R. D. Cowan, *Nature*, Los Alamos Series in Basic and Applied Sciences, Vol. 140 (University of California Press, 1981) Chap. 8 and 16, p. 626627.

[21] M. Y. Amusia, *Atomic Photoeffect* (Springer, 1990).

[22] J. E. Barnes, Journal of Computational Physics **87** (1990), 10.1016/0021-9991(90)90232-P.

[23] C. Bostedt, H. Thomas, M. Hoener, T. Mller, U. Saalmann, I. Georgescu, C. Gnodtke, and J.-M. Rost, New Journal of Physics **12** (2010), 10.1088/1367-2630/12/8/083004.

[24] T. Fennel, K.-H. Meiwes-Broer, J. Tiggesbumker, P. M. Dinh, and E. Suraud, Reviews of Modern Physics **82**,

17931842 (2010).
[25] M. Hoener, C. Bostedt, H. Thomas, L. Landt, E. Eremina, H. Wabnitz, T. Laarmann, R. Treusch, A. R. B. de Castro, and T. Mller, Journal of Physics B: Atomic, Molecular and Optical Physics **41**, 181001 (2008).
[26] B. Iwan, J. Andreasson, M. Bergh, S. Schorb, H. Thomas, D. Rupp, T. Gorkhover, M. Adolph, T. Mller, C. Bostedt, J. Hajdu, and N. Tîmneanu, Physical Review A **86** (2012), 10.1103/PhysRevA.86.033201.
[27] H. Iwayama, A. Sugishima, K. Nagaya, M. Yao, H. Fukuzawa, K. Motomura, X.-J. Liu, A. Yamada, C. Wang, K. Ueda, N. Saito, M. Nagasono, K. Tono, M. Yabashi, T. Ishikawa, H. Ohashi, H. Kimura, and T. Togashi, Journal of Physics B: Atomic, Molecular and Optical Physics **43**, 161001 (2010).
[28] M. Krikunova, M. Adolph, T. Gorkhover, D. Rupp, S. Schorb, C. Bostedt, S. Roling, B. Siemer, R. Mitzner, H. Zacharias, and T. Mller, Journal of Physics B: Atomic, Molecular and Optical Physics **45**, 105101 (2012).
[29] T. Laarmann, A. de Castro, P. Grtler, W. Laasch, J. Schulz, H. Wabnitz, and T. Mller, Physical Review Letters **92** (2004), 10.1103/PhysRevLett.92.143401.
[30] T. Laarmann, M. Rusek, H. Wabnitz, J. Schulz, A. de Castro, P. Grtler, W. Laasch, and T. Mller, Physical Review Letters **95** (2005), 10.1103/PhysRevLett.95.063402.
[31] R. Moshammer, Y. Jiang, L. Foucar, A. Rudenko, T. Ergler, C. Schrter, S. Ldemann, K. Zrost, D. Fischer, J. Titze, T. Jahnke, M. Schffler, T. Weber, R. Drner, T. Zouros, A. Dorn, T. Ferger, K. Khnel, S. Dsterer, R. Treusch, P. Radcliffe, E. Plnjes, and J. Ullrich, Physical Review Letters **98** (2007), 10.1103/PhysRevLett.98.203001.
[32] D. Rupp, M. Adolph, T. Gorkhover, S. Schorb, D. Wolter, R. Hartmann, N. Kimmel, C. Reich, T. Feigl, A. R. B. de Castro, R. Treusch, L. Strder, T. Mller, and C. Bostedt, New Journal of Physics **14**, 055016 (2012).
[33] U. Saalmann, Journal of Physics B: Atomic, Molecular and Optical Physics **43**, 194012 (2010).
[34] M. Schffler, K. Kreidi, D. Akoury, T. Jahnke, A. Staudte, N. Neumann, J. Titze, L. Schmidt, A. Czasch, O. Jagutzki, R. Costa Fraga, R. Grisenti, M. Smolarski, P. Ranitovic, C. Cocke, T. Osipov, H. Adaniya, S. Lee, J. Thompson, M. Prior, A. Belkacem, T. Weber, A. Landers, H. Schmidt-Bcking, and R. Drner, Physical Review A **78**, 013414 (2008).
[35] H. Thomas, C. Bostedt, M. Hoener, E. Eremina, H. Wabnitz, T. Laarmann, E. Plnjes, R. Treusch, A. R. B. de Castro, and T. Mller, Journal of Physics B: Atomic, Molecular and Optical Physics **42**, 134018 (2009).
[36] Z. B. Walters, R. Santra, and C. H. Greene, Physical Review A **74**, 43204 (2006), arXiv:0510187v3 [arXiv:physics].
[37] B. Ziaja, H. Wabnitz, F. Wang, E. Weckert, and T. Mller, Physical Review Letters **102** (2009), 10.1103/PhysRevLett.102.205002.
[38] B. Ziaja, H. Wabnitz, E. Weckert, and T. Mller, New Journal of Physics **10**, 043003 (2008).
[39] J. Zweiback, T. Ditmire, and M. Perry, Physical Review A **59**, R3166R3169 (1999).
[40] M. Arbeiter and T. Fennel, New Journal of Physics **13**, 053022 (2011).
[41] D. Bauer, Journal of Physics B: Atomic, Molecular and Optical Physics **37**, 30853101 (2004).
[42] C. Deiss, N. Rohringer, J. Burgdrfer, E. Lamour, C. Prigent, J.-P. Rozet, and D. Vernhet, Physical Review Letters **96** (2006), 10.1103/PhysRevLett.96.013203.
[43] F. Dorchies, T. Caillaud, F. Blasco, C. Bont, H. Jouin, S. Micheau, B. Pons, and J. Stevefelt, Physical Review E **71** (2005), 10.1103/PhysRevE.71.066410.
[44] V. P. Krainov, Journal of Physics B: Atomic, Molecular and Optical Physics **33**, 15851595 (2000).
[45] V. P. Krainov and M. B. Smirnov, Physics Reports **370**, 237331 (2002).
[46] A. Lindblad, T. Rander, I. Bradeanu, G. hrwall, O. Bjrneholm, M. Mucke, V. Ulrich, T. Lischke, and U. Hergenhahn, Physical Review B **83** (2011), 10.1103/PhysRevB.83.125414.
[47] G. N. Makarov, Uspekhi Fizicheskih Nauk **179**, 487 (2009).
[48] S. Namba, N. Hasegawa, M. Kishimoto, M. Nishikino, K. Takiyama, and T. Kawachi, Physical Review A **84** (2011), 10.1103/PhysRevA.84.053202.
[49] M. Rusek and A. Orowski, Physical Review A **71** (2005), 10.1103/PhysRevA.71.043202.
[50] U. Saalmann and J.-M. Rost, in *Photonic, Electronic and Atomic Collisions - Proceedings of the XXIV International Conference* (World Scientific Publishing Co. Pte. Ltd., Singapore, 2006) p. 160167.
[51] J. Schulz, H. Wabnitz, T. Laarmann, P. Gurtler, W. Laasch, A. Swiderski, T. Moller, and A. R. B. de Castro, Nuclear Instruments and Methods in Physics Research Section A: Accelerators, Spectrometers, Detectors and Associated Equipment **507**, 572576 (2003).
[52] C. Siedschlag and J. Rost, Physical Review A **71** (2005), 10.1103/PhysRevA.71.031401.
[53] C. Staudt and A. Wucher (1998) p. 217224.
[54] M. Wahl and A. Wucher, Nuclear Instruments and Methods in Physics Research Section B: Beam Interactions with Materials and Atoms **94**, 3646 (1994).
[55] F. Wang, E. Weckert, and B. Ziaja, Journal of Plasma Physics **75**, 289 (2008).
[56] B. Ziaja, A. R. B. de Castro, E. Weckert, and T. Mller, The European Physical Journal D **40**, 465480 (2006).
[57] B. Ziaja, H. Wabnitz, F. Wang, E. Weckert, and T. Moeller, , 4 (2008), arXiv:0810.3813.
[58] B. Ziaja, H. Wabnitz, E. Weckert, and T. Mller, EPL (Europhysics Letters) **82**, 24002 (2008).
[59] B. Ziaja, T. Laarmann, H. Wabnitz, F. Wang, E. Weckert, C. Bostedt, and T. Mller, New Journal of Physics **11**, 103012 (2009).
[60] A. de Castro, C. Bostedt, P. Grtler, T. Laarmann, W. Laasch, J. Schulz, A. Swiderski, H. Wabnitz, and T. Mller, Journal of Electron Spectroscopy and Related Phenomena **144-147**, 36 (2005).
[61] A. R. B. de Castro, C. Bostedt, E. Eremina, M. Hoener, H. Thomas, T. Laarmann, T. Fennel, K. Meiwes-Broer, E. Plnjes, M. Kuhlmann, H. Wabnitz, and T. Mller, Journal of Electron Spectroscopy and Related Phenomena **156-158**, 2529 (2007).
[62] R. von Pietrowski, K. von Haeften, T. Laarmann, T. Mller, L. Museur, and A. V. Kanaev, The European Physical Journal D **38**, 323336 (2006).